



NEUROSCIENCE

Axonal self-sorting without target guidance in *Drosophila* visual map formation

Egemen Agi^{1†}, Eric T. Reifenstein^{2†}, Charlotte Wit¹, Teresa Schneider¹, Monika Kauer¹, Melinda Kehribar¹, Abhishek Kulkarni¹, Max von Kleist^{2*}, P. Robin Hiesinger^{1*}

The idea of guidance toward a target is central to axon pathfinding and brain wiring in general. In this work, we show how several thousand axonal growth cones self-pattern without target-dependent guidance during neural superposition wiring in *Drosophila*. Ablation of all target lamina neurons or loss of target adhesion prevents the stabilization but not the development of the pattern. Intravital imaging at the spatiotemporal resolution of growth cone dynamics in intact pupae and data-driven dynamics simulations reveal a mechanism by which >30,000 filopodia do not explore potential targets, but instead simultaneously generate and navigate a dynamic filopodial meshwork that steers growth directions. Hence, a guidance mechanism can emerge from the interactions of the axons being guided, suggesting self-organization as a more general feature of brain wiring.

Target-dependent guidance of axonal growth cones is a well-studied and intuitive concept to explain the development of neuronal connections (1–3). Yet, especially in dense brain regions, a growing axon may have to navigate paths affected by its own growth and concurrently developing cells (4–7).

Visual maps, like many other brain regions, develop columns and layers that ensure local neighborhoods prior to synapse formation (5, 8–13). The *Drosophila* visual map is wired according to the principle of neural superposition (14, 15). Six photoreceptor neurons (R cells 1 to 6, herein referred to as R1–6) in each of the ~800-unit eyes (ommatidia) receive input through six different visual axes. The lamina plexus serves as a temporary sorting plane, where the growth cones (800 × 6) correct the input pattern such that the six photoreceptor neurons with the same visual axis (from six different ommatidial bundles) are sorted together into 800 new bundles (Fig. 1, A and B, and fig. S1A). All growth cones re-sort by elongating from their “heels,” which stably mark the input pattern (Fig. 1C) (16). After 15 hours of growth cone elongation (Fig. 1D), the output pattern is formed by the “fronts” of the growth cones, which subsequently grow into columns underneath the disintegrating sorting plane (Fig. 1, B and E) (17, 18).

It has remained unclear how the target lamina neurons (L cells) could provide guidance; for example, the L cells labeled “B” in the center of Fig. 1D would have to be an attractive target for an R4 growth cone from point “A” and a repulsive starting point for another R4

projecting to “C.” Yet, the growth directions of R1–6 are locally determined and not guided by a global organizing principle such as a gradient (19). Initial R1–6 growth cone extension angles are determined by the bundle from which they originate (20, 21), followed by synchronous elongation (Fig. 1, C to E) (16). How R1–6 directional growth is computed and terminated, and what role “targets” play during this process, remains unknown.

Without target L cells, R1–6 growth cones establish, but fail to stabilize, neural superposition

We genetically ablated all five subtypes of L cells by preventing their differentiation through a *smoothened* (*smo*) RNA interference (RNAi)-induced block of hedgehog signaling in lamina precursor cells (22–24) (Fig. 1, F and G). In the absence of all L cells, R1–6 growth cones established a regular pattern prior to growth cone extension [25 hours after puparium formation (hAPPF), P25] (Fig. 1, H and I). However, by the end of neural superposition sorting (P50), no columnar lamina formed underneath the disintegrating lamina plexus (Fig. 1, J to M). Hence, L cells are required at some point between initial axon arrival, growth cone extension, and the stabilization of the wiring pattern.

The sheet formed by ~4800 R1–6 growth cones bears hallmarks of an epithelial organization, including the adherens junction marker E-cadherin (ECad) that marks the points of contact between R1 to R6 heels (fig. S1B) (25). Correspondingly, we found that Armadillo (Arm), the *Drosophila* homolog of the ECad interactor β-catenin (26, 27), labeled the five points of contact between R1–6 within the bundle and additionally, all L cells (Fig. 1, H, I, N, and O). In the absence of L cells, only the Arm labeling of these contact points remained, leaving them in a circular arrangement (Fig. 1, I,

N, and O). On the basis of the bundle center and axes defined by Arm labeling, the arrangement of R1–6 bundles was largely preserved (fig. S1, C to F). Furthermore, labeling of only R4s, a single subtype that occupies a stereotypic bundle position (21, 28), revealed correct arrangements and polarization in the absence of L cells (Fig. 1, P to R). Correspondingly, sparse labeling of individual growth cones revealed indistinguishable morphologies for all R1–6 subtypes at P25 in the presence or absence of L cells (fig. S1, G and H). Therefore, lamina neurons do not contribute to the initial patterning of the lamina plexus other than occupying space within the R1 to R6 growth cone pattern.

To investigate the dynamics of R1–6 extensions, we used noninvasive, intravital live imaging in intact pupae; we first imaged R4s together with L cells (movie S1). Both in the presence and absence of L cells, we observed similar R4 morphologies and extension dynamics at the correct angle until ~P35 (Fig. 2, A and B, and movie S2). After P35, R4s started to aberrantly fork, bend, or retract in the absence of L cells (materials and methods) (Fig. 2C). Analyses of all R1–6 subtypes from fixed and live preparations at P35 also revealed similar extension angles, lengths, and overlap with the correct target regions both in the presence and absence of L cells (Fig. 2, D to F). Hence, the initial neural superposition pattern is established by P35 with or without L cells.

These data suggest the possibility that a sheet of R1–6 growth cones self-organizes into the neural superposition pattern without the aid of other cell types. However, although we found no evidence for other neuronal or glial processes in the developing lamina plexus (fig. S2, A to E), the roles of other cells are difficult to exclude. Fortunately, when studying the role of *arm*, we found that R1–6 growth cone sheets can also form in ectopic brain regions (Fig. 2, G to I). Panneuronal *arm* RNAi expression causes a well-known *wingless* phenotype in dorsoventral patterning of cells in the region targeted by photoreceptor axons (29). This anatomical disruption caused a large segment of photoreceptor axons to detach from the optic stalk and terminate in one or more ectopic regions, predominantly dorsal of the medulla (arrow, Fig. 2G, and fig. S3, A and L), where neurons, lamina precursors, or glia cells are highly variable, disorganized, and sometimes completely absent (Fig. 2, H and I, and fig. S3, B and C). Despite these variable surroundings, ectopic photoreceptor axons formed a regular growth cone sheet (Fig. 2, J to L), including stereotypic R4 positions (Fig. 2J and fig. S3, D to F, H to J, and M). The R4 growth cones were initially polarized correctly and elongated between P25 and P30 [Fig. 2, J (right) and L], although the polarization angles

¹Division of Neurobiology, Free University of Berlin, 14195 Berlin, Germany. ²Department of Mathematics, Free University of Berlin, 14195 Berlin, Germany.

*Corresponding author. Email: vkleist@zedat.fu-berlin.de (M.v.K.); robin.hiesinger@fu-berlin.de (P.R.H.)

†These authors contributed equally to this work.

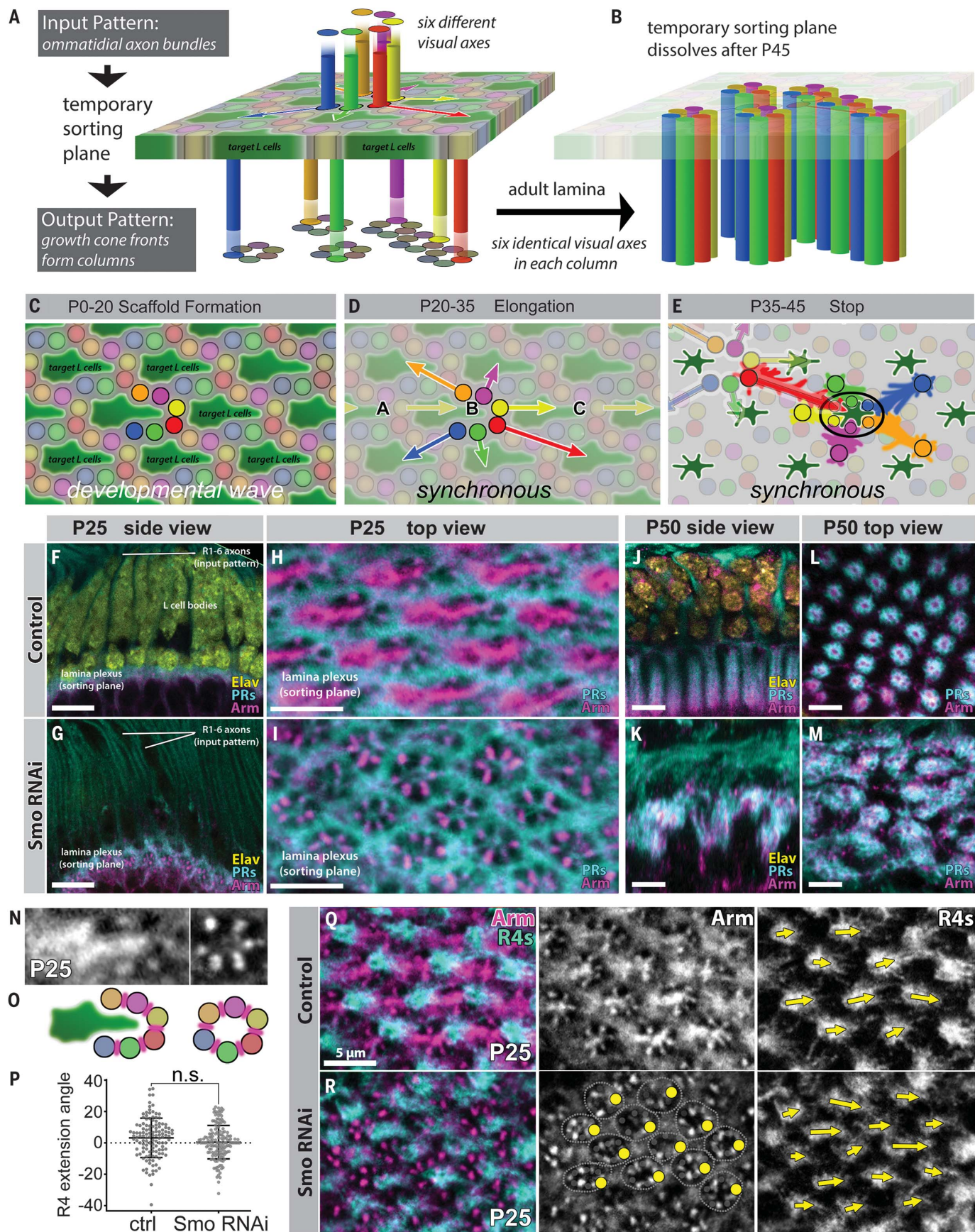


Fig. 1. R1–6 form a highly organized growth cone sheet in the absence of L cells. (A) Schematic of the development of neural superposition in a temporary

sorting plane, the lamina plexus. Each of six outer photoreceptors (R1–6, color-coded as blue, green, red, yellow, magenta, and orange in order) in an ommatidium receives input through a different visual axis, whereas R1–6 from six different ommatidia have the same visual axis. The ommatidial input pattern is corrected to the neural superposition output pattern in an intricate axonal resorting process. (B) The output pattern is preserved in the lamina, a columnar neuropil below the sorting plane, which disintegrates after P45. (C to E) Timeline of neural superposition development in the temporary sorting plane. (C) Photoreceptors arrive in the lamina plexus following their wave of differentiation in the retina until P20. (D) Between P20 and P35, all R1–6 growth cones elongate within the sorting plane synchronously while their original arrival points (heels) remain stably anchored. (E) R1–6 growth cone fronts from six different bundles form the output pattern with their fronts surrounding L-cell clusters (green). (F to I) Patterned sheet of R1–6 growth cones in the control [(F) and (H)] and *smo*

RNAi-mediated L-cell ablation [(G) and (I)] at the beginning of neural superposition sorting (P25). Cyan, R1–6 axons (photoreceptors, PRs); magenta, Arm (Armadillo, β -catenin) labeling of L cells and R1–6 junctions; yellow, Elav (pan-neuronal nuclear marker) labeling of L-cell bodies. $n \geq 5$ optic lobes. Scale bars, 10 μm [(F) and (G)] and 5 μm [(H) and (I)]. (J to M) Visual map formation after neural superposition development (P50) in the control [(J) and (L)] and without L cells [(K) and (M)]. $n \geq 5$ optic lobes. Scale bars, 8 μm (J) and 5 μm [(K) to (M)]. (N and O) Ommatidial bundle organization in the absence of L cells based on Arm labeling. Bundles in (N) are from (H) and (I). (P to R) (P) Quantification of R4 extension angles. Pattern formation and growth cone extension angles of the single subtype R4 in the control (Q) and in the absence of L cells (R). Cyan, R4 growth cones; magenta, Arm labeling of L cells and R1–6 junctions. $n = 124$ (six optic lobes) for control, $n = 161$ (seven optic lobes) for *smo* RNAi. Unpaired *t* test with Welch's correction; n.s., not significant. Error bars in (P) represent mean \pm SD. Scale bars, 5 μm .

were more variable than in the lamina plexus (Fig. 2K).

Feedback among R1–6 growth cones self-corrects extension angles independent of the presence, absence, or heterogeneous collapse of the L-cell pattern

In the wild type, all six R-cell growth cones and all five L-cell subtypes span the full ~3- μm thickness of the temporary sorting plane and thereby contribute to its pattern (R4, Fig. 3A; all subtypes, fig. S4). We created a heterogeneously distorted sorting plane using a sparse L-cell ablation (or “killing”) approach (Fig. 3B) (materials and methods) and followed the progressive deterioration of the remaining L-cell pattern (Fig. 3, C to F, and movie S2). Irregular overlaps of nonablated L cells across columns were already obvious at P25, indicating aberrant interactions (Fig. 3, D and F). By P35, irregular overlaps had reached an extent that obscured the original columnar pattern. At the same time, R4 growth cone extensions were almost error free, irrespective of the progressively collapsing L-cell pattern (Fig. 3, D and F).

Previous work suggested that elongating R1–6 growth cones from a single ommatidial bundle maintain fixed extension angles based on their initial polarization (16, 21). However, a self-organizing process would require feedback between the locally interacting components (30). We devised a test for feedback based on the variability of input bundle rotations, which reached 20° in either direction in the wild type and in the complete or partial absence of L cells (Fig. 3, G to J). As shown in Fig. 3, K to M, R4 extension angles exhibited precise corrections of their extension angles both in the presence and absence of L cells. This self-correction of growth cone extensions relative to the surroundings suggests feedback between R cells across bundles.

R1–6 filopodia do not sense targets, but generate a self-patterning meshwork around them

Growth cones sense their environment with dynamic filopodia that play important roles in

axon guidance (31). But it remains unclear what type of guidance a growth cone receives when the only interaction partners are other extending growth cones. R cell-specific membrane labeling revealed a patterned filopodial meshwork that excluded both the starting points of growth cone extension (R cell heels; yellow discs in Fig. 4A, bottom left) and all presumptive target regions (L cells; green discs in Fig. 4A, bottom left) (examples, Fig. 4, A to C; all subtypes at all timepoints, fig. S5). Correspondingly, only <10% of filopodia tips localized to target regions, and ~90% localized within the filopodial meshwork; these numbers remained largely unchanged from P25 to P40 (Fig. 4D).

Using an improved two-photon imaging method, we obtained up to 2-min time-lapse of individual growth cones at P25, P30, P35, and P40, as shown in movie stills for a single R1 (Fig. 4, E to H, and movie S3) and a single R3 (Fig. 4, I to L, and movie S3). We traced all filopodia (red vectors, Fig. 4, E to L) and calculated the growth cone “front” as the crossing point of front filopodial vector origins (red dots, Fig. 4, E to L) (materials and methods). The newly defined vector from the growth cone heel to this calculated front (blue dots and blue vectors, Fig. 4, E to L) recapitulated the slow R1–6 growth cone extension between P25 and P40 (Fig. 2F).

Filopodial tip exploration over a period of 1 hour exhibited no preference for target regions, as shown for one individual growth cone of each subtype at P30 in Fig. 4M (all time points, fig. S6). Instead, filopodia predominantly explored areas around the target regions. An analysis of R1–6 filopodia in the absence of L cells based on fixed samples revealed similar distributions (fig. S7). Calculated length-weighted averages of all R1–6 filopodia that emerged over a 1-hour period matched the direction of growth cone extension from heel to front (compare vectors, Fig. 4N; blue vectors, Fig. 4, E to L; Fig. 2, D to F; and fig. S8, E and F), as suggested by previous work (21). Analysis of fixed R1–6 growth cones in the absence of L cells revealed similar angular distributions (gray graphs, Fig. 4N; and fig. S8, G and H).

These data suggest a mechanism in which ~30,000 to ~48,000 filopodia generate the sorting plane while defining a direction of growth for each of the ~4800 R1–6 growth cones in the presence or absence of L cells. First, filopodia generate a meshwork around all presumptive target regions (Fig. 4, M and N). Second, the averaged vector of filopodial meshwork exploration “guides” the slow extension of the growth cone fronts. Crucially, the integration of fast filopodial meshwork exploration yields a stable vector for the slow growth cone elongations. Indeed, both filopodial numbers and lengths changed little between P25 to P40, thereby maintaining a stable meshwork despite continuous filopodia extensions and retractions (fig. S8, A and C). Filopodia tips remained 2 to 4 μm away from the target regions at all time points (fig. S8B). Quantification of R1–6 filopodia in the absence of L cells based on fixed samples between P25 to P35 revealed very similar dynamics, with lengths reduced proportionally to the size of the sorting plane (fig. S8, A to D).

Each growth cone is effectively generating and navigating the self-organizing filopodial meshwork together with ~4800 other growth cones undergoing the same process. At P25, individual growth cones explored a region overlapping with 24 to 32 other R1–6 growth cones, with numbers almost evenly distributed amongst R1–6 subtypes (fig. S9A). The number of overlaps was reduced to 12 to 17 by P35, while maintaining interactions with all subtypes. Analogous calculations in the absence of L cells yielded similar results (fig. S9B). We quantified this nonspecificity of filopodial interactions in terms of entropy, whereby specific interactions denote low entropy, and interactions with all subtypes, maximum entropy; all R1–6 growth cones exhibited close to maximum entropy throughout neural superposition sorting (Fig. 4O).

Target L cells are passive adhesion sinks

L cells were previously shown to mediate attractive interactions with R1–6 growth cones

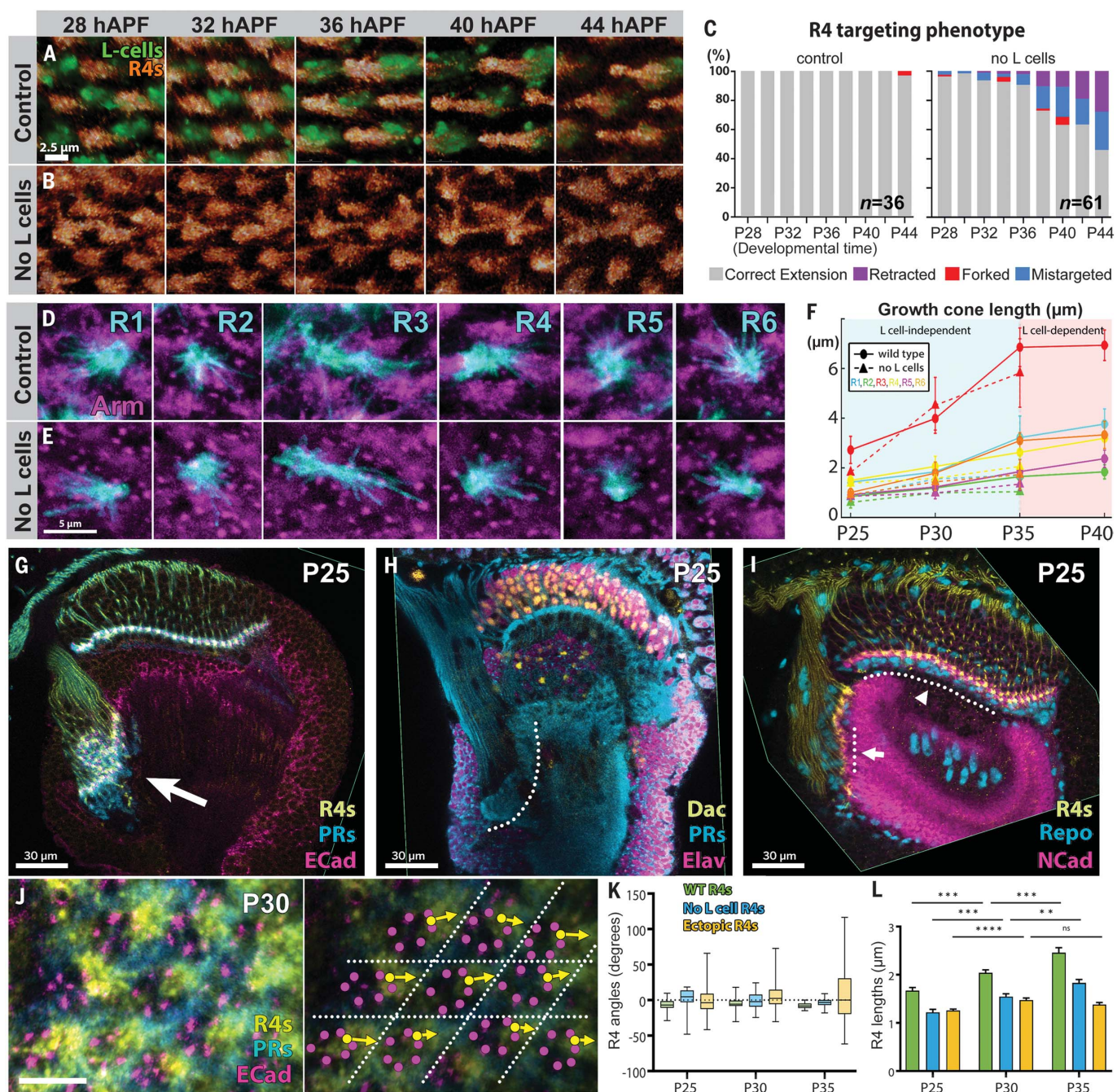


Fig. 2. R1–6 growth cones establish the neural superposition wiring pattern in the absence of L cells. (A to C) Intravital live imaging of R4 growth cones in the sorting plane in the control (A) and in the absence of L cells (B). Quantification of the stabilization phenotype is shown in (C). $n = 36$ R4s from one intravital live imaging experiment for the control; $n = 61$ R4s from three intravital live imaging experiments for “no L cells.” Scale bars, 2.5 μm . (D and E) All R1–6 subtypes morphologies at P35 in the presence (D) or absence (E) of L cells. Growth cones shown in the cyan channel in (E) have been manually segmented to remove neighboring growth cones. $n = 4$ to 7 growth cones for each subtype. Scale bars, 5 μm . (F) Quantification of R1–6 growth cone lengths over time in the presence (wild type) and absence of L cells. Wild-type R1–6 lengths were derived from intravital live imaging datasets, and R1–6 lengths in the absence of L cells were derived from stochastically labeled fixed brains. For the wild type, $n = 4$ to 13 for each subtype at all time points from four intravital live imaging experiments. For “no L cells,” $n = 3$ to 7 for each subtype at all time points from 18 (P25),

12 (P30), and 14 (P35) optic lobes. Error bars represent the mean \pm SD. (G to L) Analysis of ectopic R1–6 growth cone sheets [arrows in (G) and (I)] induced by arm RNAi. (G) Yellow, R4s; cyan, R1–6; magenta, ECad. (H) Yellow, Dac (transcription factor in lamina precursor cells and lamina neurons); cyan, R1–6; magenta, Elav. (I) Yellow, R4s; cyan, Repo (all glia nuclei); magenta, NCad. Glia layers sandwich the lamina plexus (arrowhead) but not the ectopic growth cone sheet (arrow). (J) High-resolution cross-section of the ectopic R1–6 growth cone sheet at P30. Yellow, R4s; cyan, R1–6; magenta, R1–6 junctions marked with ECad. (Right) Same section as in (J) but with R4 heel positions and polarization vectors marked (yellow discs and vectors). [(K) and (L)] R4 extension angles (K) and lengths (L) over time in the wild type, “no L cell” clones, and in ectopic growth cone sheets. $n \geq 4$ optic lobes for [(G) to (J)]. $n \geq 30$ growth cones for all groups at all time points [(K) and (L)]. Statistics as described in materials and methods; *** $P < 0.0001$; ** $P < 0.001$; * $P < 0.01$; ns, not significant. Error bars in (L) represent the mean \pm SEM. Scale bars, 30 [(G) to (I)] and 5 μm (J).

based on experiments where the cell adhesion molecule N-Cadherin (NCad) was removed from L cells (25, 32). We used the same meth-

od (32) and performed both fixed and intravital imaging of wild type R1–6 with mutant L cells. Scaffold formation and extension of

R4 growth cones were indistinguishable from control until P35 (Fig. 4P, fig. S10, A and B and movie S4). Thereafter, individual R4s exhibited

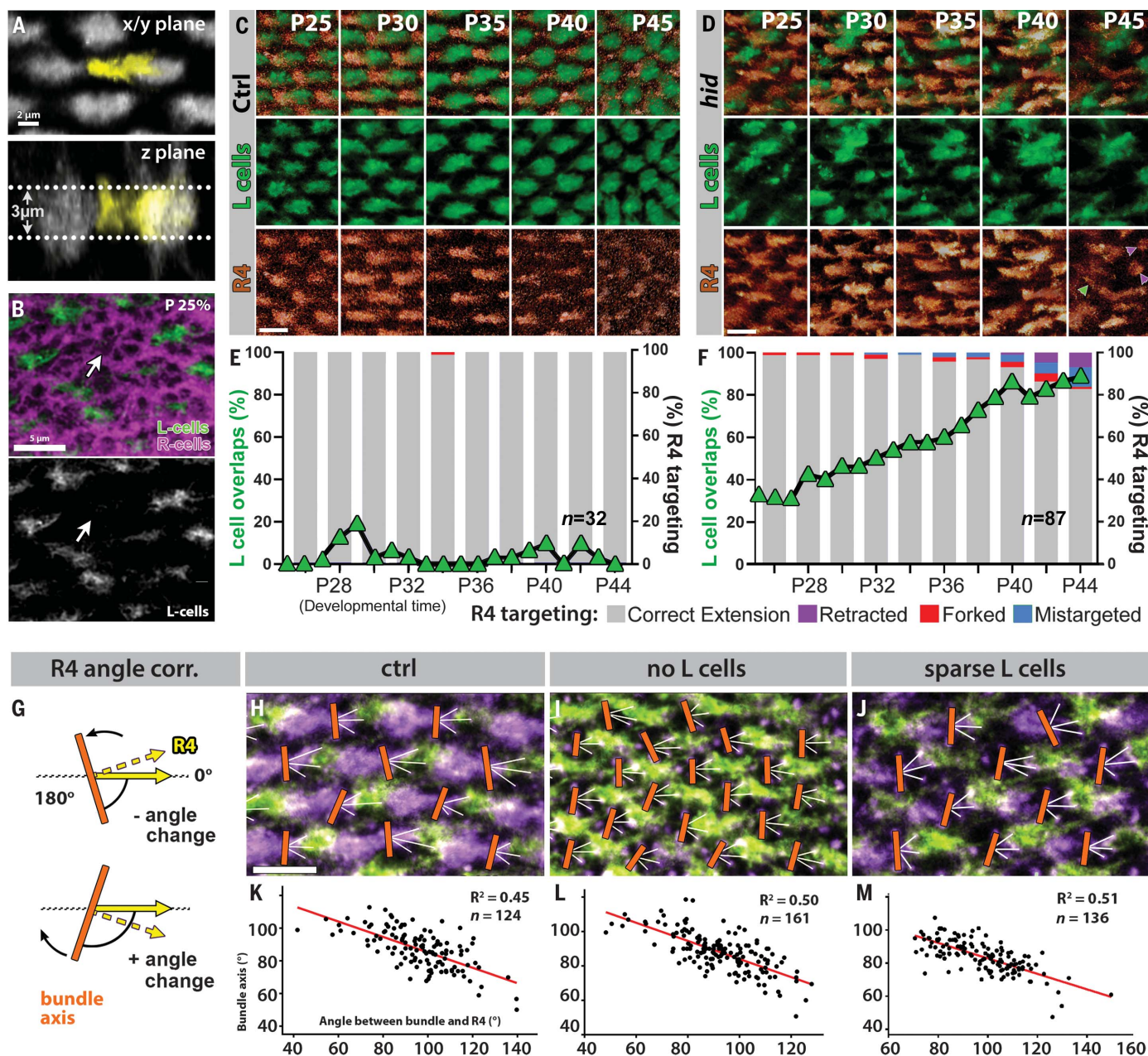


Fig. 3. Feedback among R1-6 growth cones generates a self-correcting meshwork independent of the presence, absence, or heterogeneous collapse of the L-cell network. (A) The ~3-μm-thick R1-6 growth cone sheet at P35. An R4 from an intravital imaging dataset is shown in yellow, and L-cell neurites are shown in grayscale. See fig. S4 for all subtypes and time points. (B) Heterogeneous sorting plane at P25 after sparse L-cell killing. The arrows indicate an ommatidial R1-6 bundle without any L cells. (Top) R cells, magenta; L cells, green. (Bottom) L cell-only single channel. $n = 5$ optic lobes. (C to F) Intravital live imaging of R4s (brown) together with L cells (green) in control (C) and sparse L-cell ablation conditions (D). In (D), fully retracted and missorted R4s are indicated by magenta and green arrowheads, respectively. *hid*, head involution defective-induced apoptosis. Quantifications of L-cell cluster overlaps and the R4 targeting phenotype in the control and heterogeneous

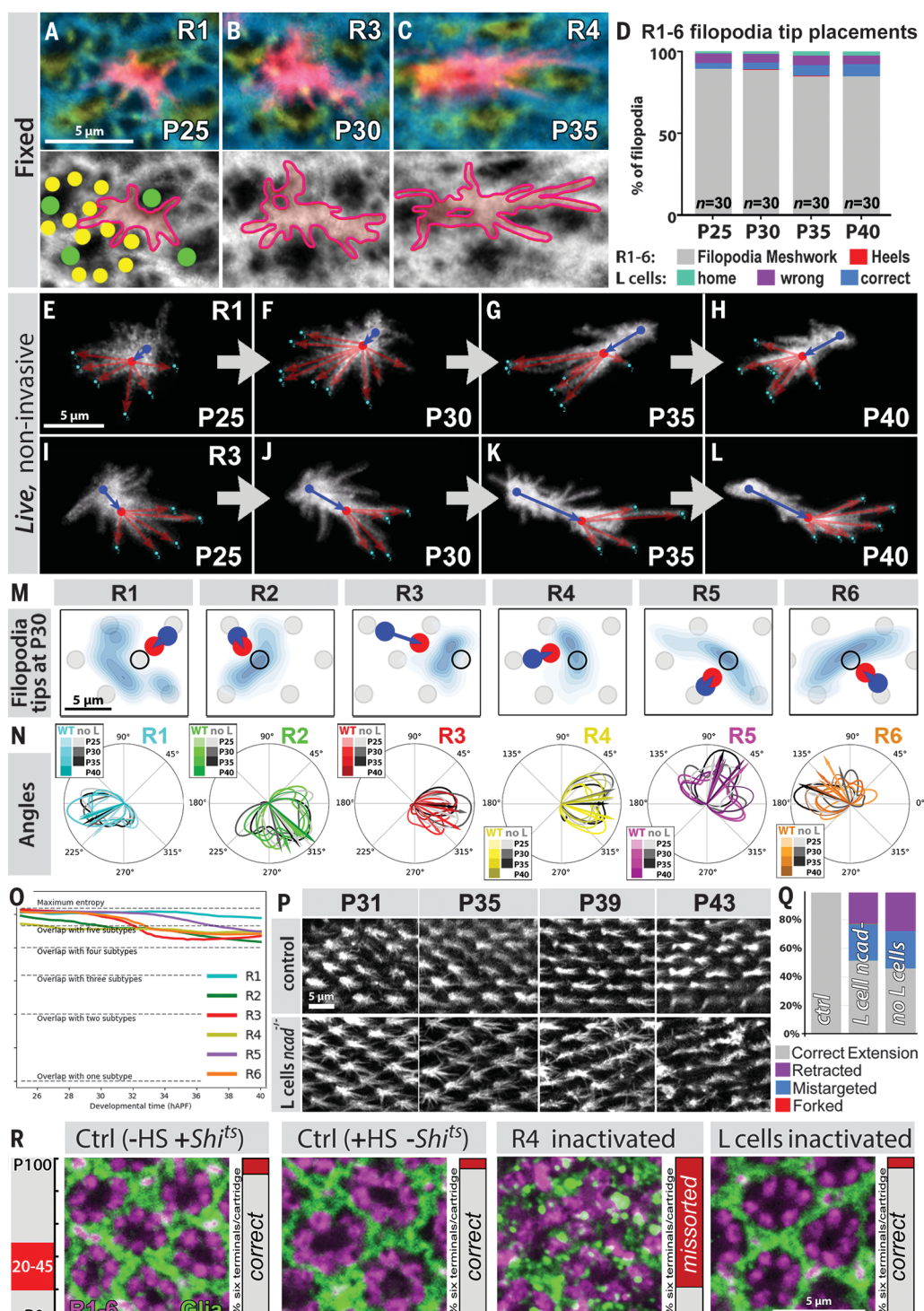
laminae are shown in (E) and (F), respectively. $n = 32$ R4s from one intravital live imaging experiment for control; $n = 87$ R4s from one intravital live imaging experiment for sparse L-cell killing. (G to M) Correction of R1-6 growth cone extension angles. (G) Self-correction is quantified as the stability of R4 extension at 0° (yellow arrow) despite variable R1-6 bundle orientations. [(H) to (J)] Qualitative and quantitative variability of the orientations of individual incoming R1-6 bundles in the control (H), L-cell absence (I), and sparse L-cell killing (J) conditions, as determined by Arm labeling (magenta). R4s are marked in yellow. [(K) to (M)] Quantification of the bundle axis versus the angle between the bundle and the R4 extension direction. Negative correlations for all conditions reveal self-correction of R4 extension angles. (K) $n = 124$ (six optic lobes), $R^2 = 0.45$, Pearson, one-tailed; (L) $n = 161$ (seven optic lobes), $R^2 = 0.50$, Pearson, one-tailed; (M) $n = 136$ (five optic lobes), $R^2 = 0.51$, Pearson, one-tailed.

Fig. 4. R1–6 filopodia do not sense targets but follow paths they themselves generate in a self-patterning filopodial meshwork.

(A to D) Meshwork formed by R1–6 growth cone filopodia. [(A) to (C)] Representative examples of single R1–6 growth cones (magenta) at different time points that align with total-membrane labeling of the filopodial meshwork (top, blue channel; bottom, single channel). The filopodial meshwork excludes R1–6 heels [(A) bottom, yellow discs] and L cells [(A) bottom, green discs]. For all subtypes and time points, see fig. S5. (D) Quantification of R1–6 filopodia tip localization in the lamina plexus at four different time points during neural superposition wiring. $n = 30$ (five of each subtype). Equator to the right, posterior down. (E to L) Snapshots of a single R1 [(E) to (H)] and a single R3 [(I) to (L)] growth cone from intravital imaging through time (movie S3). Blue discs, growth cone heels; red discs, growth cone fronts (origin of all front filopodia); blue vectors, heel-to-front axis; red vectors, front filopodia. (M) Spatial distribution of R1–6 front filopodia tips at P30, each over a 1-hour period (2- to 5-min time-lapse). Filopodia tip distributions are shown as blue clouds in a target grid. See fig. S6 for all subtypes at all time points. Blue discs, growth cone heels; blue vectors, heel-to-front axis; black circle, correct target; gray discs, all targets. $n \geq 60$ filopodia of single growth cones for each subtype.

(N) R1–6 front filopodia angular distributions in the wild type (colored graphs) and absence of L cells (gray-scale graphs). For wild-type conditions, filopodia measurements covered 1-hour periods at a 2- to 5-min time-lapse throughout superposition sorting from P25 to P40. For “no L cell” conditions, filopodia of multiple fixed growth cones were measured during the L cell-independent phase at P25, P30, and P35. Vectors show the weighted vector average of all measured filopodia for a subtype and timepoint. $n \geq 14$

filopodia for each time point and subtype in wild-type and “no L cell” conditions. (O) Filopodia overlap entropy as a measure of R1–6 filopodia interaction specificity. Filopodial exploration based on measured parameters (N) (fig. S8) of any R1–6 overlaps with filopodia of all subtypes (fig. S9). Colored lines depict these subtype-specific entropies as a function of time. The dashed horizontal lines show the theoretically expected entropy for the uniform overlap of a given growth cone with 1 to 6 subtypes. (P) Intravital live imaging of R4s in the control (top) and after *ncad* reduction (“knockdown”) in L cells (bottom). (Q) Quantification of R4 wiring errors for loss of NCad in L cells and complete loss of L cells at P43 (± 1 hour). $n = 51$ R4s from one intravital live imaging experiment for control; $n = 175$ R4s from three intravital live imaging experiments for *ncad* RNAi; $n = 61$ R4s from three intravital live imaging experiments for “no L cells.” (R) Effects of a cell type-specific block of membrane dynamics between P20 and P45 on the adult R1–6 output pattern in the lamina. Magenta, R1–6 axonal terminals; green, epithelial glia. Quantification of the percentage of cartridges with six R1–6 axon terminals in quantification bars on the right. Correct = six terminals; missorted \neq six terminals. $n = 251$ cartridges (eight optic lobes) for control [-Heat Shock (HS), +*shibire*^{ts} (*Shi*^{ts})]; $n = 174$ cartridges (six optic lobes) for control (+HS, -*Shi*^{ts}); $n = 96$ cartridges (three optic lobes) for R4 inactivated; $n = 284$ cartridges (eight optic lobes) for L cells inactivated.



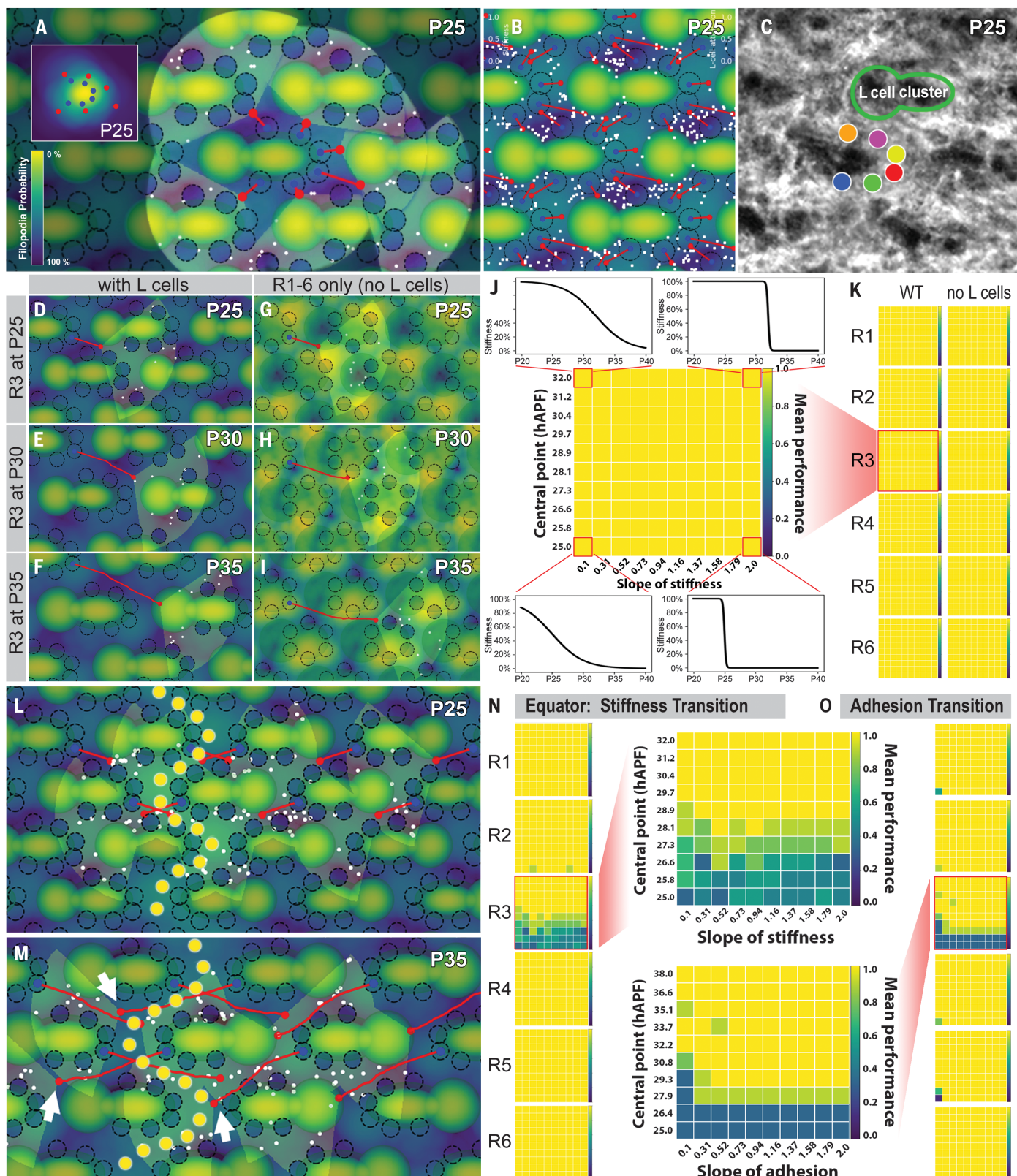


Fig. 5. A comprehensive computational model and filopodial dynamics simulation of neural superposition reveals sufficiency and robustness of R1–6 axonal self-sorting. (A) Computational model and simulation of R1–6 growth cones at P25. (Inset) The density gradient of a single bundle is shown. The density landscape of the sorting plane was computed from R1–6 growth cone densities based on intravitral imaging and quantitatively reflects the probability of filopodia tips' localization (see fig. S12, A and B, for densities of individual subtypes and bundles at all time points). Blue discs, heels; red discs, fronts; white dots, filopodial tips. (B) Snapshot of a simulation of all R1–6 growth cones (movie S6). (C) Expansion microscopy of a single section of the R1–6 filopodial meshwork labeled with membrane-tagged green

based on intravitral imaging and quantitatively reflects the probability of filopodia tips' localization (see fig. S12, A and B, for densities of individual subtypes and bundles at all time points). Blue discs, heels; red discs, fronts; white dots, filopodial tips. (B) Snapshot of a simulation of all R1–6 growth cones (movie S6). (C) Expansion microscopy of a single section of the R1–6 filopodial meshwork labeled with membrane-tagged green

fluorescent protein (CD4-tdGFP). $n > 5$ optic lobes. (D to I) Simulations of a R3 extension at P25, P30, and P35 with [(D) to (F)] and without L cells [(G) to (I)]. For all subtypes at all timepoints with and without L cells, see fig. S5 and movie S6, and fig. S13 and movie S7, respectively. (J and K) Simulations ($n = 10$ for each of the 100 settings) of all biologically plausible stiffness transitions, that is, the

transition from the measured initial polarization to filopodia-steered navigation. (L to O) Simulations of R1–6 self-wiring across the mirror-symmetric equator region. Snapshots for R3 at P25 (L) and P35 (M); all subtypes at all time points can be seen in movie S9. Simulations of robustness of R1–6 extensions at the equator for stiffness transitions (N) and L cell-mediated adhesion (O).

progressive destabilization, resulting in an ~50% error rate by P45 (Fig. 4Q; fig. S10C), which is very similar to complete L cell removal (Fig. 4Q). We conclude that NCad in L cells is required for the stabilization of the wiring pattern after P35.

To test whether L cells actively ‘capture’ R1–6 fronts or function as passive adhesion sinks, we disrupted L-cell membrane dynamics between P20 and P45 by using the temperature-sensitive dynamin mutant *shibire^{ts}* (33). *shibire^{ts}* reversibly disrupts membrane endocytosis (34, 35) and has been widely used to disrupt cellular development and function (36, 37). Intravital imaging of L-cell dynamics at the restrictive temperature between P20 and P45 revealed a complete loss of filopodial dynamics (fig. S11A and movie S5). In contrast to L-cell ablation or loss of NCad, this temporally restricted disruption of L-cell dynamics is acutely reversible and thus allows for continued unperturbed development and analysis of the adult outcome. Remarkably, block of membrane dynamics throughout superposition sorting between P20 and P45 in L cells had no effect on the adult pattern (Fig. 4R and fig. S11, D, E, and G to J). By contrast, block of membrane dynamics in R1–6 (fig. S11F) or only R4 led to a complete disruption of the adult visual map (Fig. 4R). These findings indicate that filopodial or membrane receptor dynamics in L cells are not required for the stabilization of the R1–6 neural superposition pattern, suggesting that L cells function as passive adhesion sinks.

A computational model reveals sufficiency and robustness of target-independent axonal self-sorting

We developed a data-driven computational model with the twin goals of testing sufficiency and robustness of the self-sorting mechanism. On the basis of measured data, we first generated a model of the dynamically changing landscape of densities and hence, spatial probabilities, of filopodia exploration for the entire growth cone sheet in time [Fig. 5, A and B (for P25); fig. S12, A to F; and movie S3]. Next, we simulated individual R1–6 growth cones in the dynamically changing density landscape based on measured growth cone front localizations (fig. S12G) and filopodia numbers, lengths, and angles (Fig. 4, M and N, and fig. S8, A and C). The resulting distribution of filopodia throughout time revealed a notably homogenous meshwork, despite the shifting growth cone front positions from which all filopodia originate (Fig. 5B). This

meshwork resembled the biological structure as seen with high-resolution expansion microscopy (Fig. 5C).

Data-driven simulations showed that filopodia-steered navigation was indeed sufficient to slowly move all R1–6 fronts to their correct target regions by P35 (Fig. 5, D to F, and movie S6). Turning on an adhesive force for all growth cone fronts (but not for filopodia) at P35 in all L cells stabilized the correct pattern. Next, we simulated the sorting plane without L cells and therefore without the corresponding exclusion zones or target adhesive forces. In the absence of L cells, the sorting plane retained a stable size (fig. S12H), and R1–6 formed a meshwork with heel regions alone defining the “no go” zones (movie S7). Notably, all R1–6 fronts extended correctly until P35 in the absence of L cells (Fig. 5, G to I; all subtypes, fig. S13 and movie S7).

We next tested the robustness of the self-sorting mechanism, starting with the transition of initial R1–6 polarization to filopodia-steered navigation, a parameter that we could not measure *in vivo* (materials and methods) (fig. S14A). R1–6 fronts arrived in the correct target regions (fig. S14, B and C) in the presence or absence of L cells without any errors for all tested values (Fig. 5, J and K). Similarly, the model was robust against the measured variability of initial polarization angles in the presence or absence of L cells (fig. S15), and the timing of adhesion when L cells were present (fig. S16A). Increasing adhesion leads to a bend of the growth cone front between P35 and P40, similar to biological observations (compare Fig. 4, K to L, with fig. S16, B to D). Next, we tested perturbations that are difficult or impossible in biology, including reducing filopodia numbers (fig. S17A), increasing filopodial lifetimes (fig. S17B), and random ablation of large numbers of growth cones without disrupting the heel grid (fig. S17, C and D). In all cases, we found that only R3, which traverses two bundle diameters, is sensitive to these perturbations, but only under conditions not normally observed in the wild type. Non-specific R1–6 filopodial interactions enabled the self-organization underlying this robustness (movie S8 and fig. S17D).

We also tested the robustness of the self-sorting mechanism for a naturally occurring perturbation: a randomly zigzagged axis that divides the lamina plexus into two mirror-symmetric halves. At this so-called equator, filopodial densities increased substantially across several bundle diameters, because target

regions received up to eight R1–6 axon terminals (Fig. 5, L and M; fig. S18, A and B; and movie S9). All subtypes robustly targeted correctly by P35, with occasional R3s not fully reaching the target across the equator (arrows, Fig. 5M), similar to historic reconstructions from flies (38, 39). R1–6 self-sorting across the equator was robust to starting angle variations (fig. S18C) and L cell-mediated adhesion starting at P28 or later (Fig. 5O and fig. S18, C and D).

Discussion

The neural superposition wiring pattern is specific to the fly, but the absence of a fixed target to steer by is likely a more general phenomenon during brain development across systems. In particular, axon–axon interactions have been shown to contribute to pathfinding (40–44). Navigation through the developing brain may less resemble address identification in a fixed city grid than the navigation of a city under construction, where the final address may not exist at the beginning of the journey (45). Although model systems with relatively stable targets have traditionally been a focus of study that allowed seminal discoveries of guidance mechanisms (1, 46), they may represent only a subset of neuronal growth decisions in the developing brain.

The self-sorting of the fly visual map is an example of a true self-organization process, or in other words, a process in which a global pattern emerges solely from the interactions of lower-level components without information or reference to the global level (30, 47, 48). We propose that the self-organization mechanism presented in this work cannot be explained through the function of a single molecular mechanism. Instead, a composite of molecular and subcellular features in time leads to the observed growth cone behavior, and only this composite of features constitutes the mechanism (49). These features include non-cell-autonomous properties such as the initial polarization angle (21) and cell-autonomous properties such as subtype-specific extension speeds (50). We suggest that such composite instructions may underlie choices for directed growth and synapse formation more commonly in developing brains.

REFERENCES AND NOTES

1. A. Chédotal, *Nat. Rev. Neurosci.* **20**, 380–396 (2019).
2. L. E. McCormick, S. L. Gupton, *Curr. Opin. Cell Biol.* **63**, 11–19 (2020).
3. J. M. Dorskind, A. L. Kolodkin, *Curr. Opin. Neurobiol.* **66**, 10–21 (2021).

4. M. Petrovic, D. Schmucker, *BioEssays* **37**, 996–1004 (2015).
5. E. Agi, A. Kulkarni, P. R. Hiesinger, *Curr. Opin. Neurobiol.* **63**, 1–8 (2020).
6. B. A. Hassan, P. R. Hiesinger, *Cell* **163**, 285–291 (2015).
7. S. Yogeve, K. Shen, *Annu. Rev. Cell Dev. Biol.* **30**, 417–437 (2014).
8. S. J. Cook, C. A. Kalinski, O. Hobert, *Curr. Biol.* **33**, 2315–2320, e2 (2023).
9. M. W. Moyle et al., *Nature* **591**, 99–104 (2021).
10. A. L. Kolodkin, P. R. Hiesinger, *Curr. Opin. Neurobiol.* **42**, 128–135 (2017).
11. J. Cang, D. A. Feldheim, *Annu. Rev. Neurosci.* **36**, 51–77 (2013).
12. J. R. Sanes, S. L. Zipursky, *Neuron* **66**, 15–36 (2010).
13. J. Malin, C. Desplan, *Proc. Natl. Acad. Sci. U.S.A.* **118**, e2101823118 (2021).
14. V. Braiterberg, *Exp. Brain Res.* **3**, 271–298 (1967).
15. O. Trujillo-Cenóz, *J. Ultrastruct. Res.* **13**, 1–33 (1965).
16. M. Langen et al., *Cell* **162**, 120–133 (2015).
17. I. A. Meinertzhagen, K. E. Sorra, *Prog. Brain Res.* **131**, 53–69 (2001).
18. P. R. Hiesinger et al., *Curr. Biol.* **16**, 1835–1843 (2006).
19. T. R. Clandinin, S. L. Zipursky, *Neuron* **28**, 427–436 (2000).
20. P. L. Chen, T. R. Clandinin, *Neuron* **58**, 26–33 (2008).
21. T. Schwabe, H. Neuert, T. R. Clandinin, *Cell* **154**, 351–364 (2013).
22. Z. Huang, S. Kunes, *Cell* **86**, 411–422 (1996).
23. V. M. Fernandes, Z. Chen, A. M. Rossi, J. Zipfel, C. Desplan, *Science* **357**, 886–891 (2017).
24. D. Umetsu, S. Murakami, M. Sato, T. Tabata, *Development* **133**, 791–800 (2006).
25. S. Prakash, J. C. Caldwell, D. F. Eberl, T. R. Clandinin, *Nat. Neurosci.* **8**, 443–450 (2005).
26. B. Riggelmann, P. Schedl, E. Wieschaus, *Cell* **63**, 549–560 (1990).
27. T. Harumoto et al., *Dev. Cell* **19**, 389–401 (2010).
28. M. T. Cooper, S. J. Bray, *Nature* **397**, 526–530 (1999).
29. K. Kaphingst, S. Kunes, *Cell* **78**, 437–448 (1994).
30. S. Camazine, J.-L. Deneubourg, N. R. Franks, *Self-Organization in Biological Systems*, Princeton Studies in Complexity (Princeton Univ. Press, 2003), pp. 548.
31. C. B. Wit, P. R. Hiesinger, *Semin. Cell Dev. Biol.* **133**, 10–19 (2023).
32. T. Schwabe, J. A. Borycz, I. A. Meinertzhagen, T. R. Clandinin, *Curr. Biol.* **24**, 1304–1313 (2014).
33. T. Kitamoto, *J. Neurobiol.* **47**, 81–92 (2001).
34. P. De Camilli, K. Takei, P. S. McPherson, *Curr. Opin. Neurobiol.* **5**, 559–565 (1995).
35. M. S. Chen et al., *Nature* **351**, 583–586 (1991).
36. M. M. Swanson, C. A. Poodry, *Dev. Biol.* **84**, 465–470 (1981).
37. P. T. Gonzalez-Bellido, T. J. Wardill, R. Kostyleva, I. A. Meinertzhagen, M. Juusola, *J. Neurosci.* **29**, 14199–14210 (2009).
38. G. A. Horridge, I. A. Meinertzhagen, *Proc. R. Soc. London Ser. B* **175**, 69–82 (1970).
39. I. A. Meinertzhagen, *Brain Res.* **41**, 39–49 (1972).
40. A. Bulfone et al., *Neuron* **21**, 1273–1282 (1998).
41. T. Imai et al., *Science* **325**, 585–590 (2009).
42. L. B. Sweeney et al., *Neuron* **53**, 185–200 (2007).
43. P. Suettelin, U. Drescher, *Neuron* **84**, 740–752 (2014).
44. F. Bonhoeffer, J. Huf, *Nature* **315**, 409–410 (1985).
45. P. R. Hiesinger, *The Self-Assembling Brain. How Neural Networks Grow Smarter* (Princeton Univ. Press, 2021), p. 384.
46. T. Xiao et al., *Cell* **146**, 164–176 (2011).
47. E. Karsenti, *Nat. Rev. Mol. Cell Biol.* **9**, 255–262 (2008).
48. C. Curantz, M. Manceau, *Curr. Opin. Genet. Dev.* **69**, 147–153 (2021).
49. P. R. Hiesinger, *BioEssays* **43**, e2000166 (2021).
50. W. Ji, L. F. Wu, S. J. Altschuler, *PLOS Genet.* **17**, e1009857 (2021).
51. E. Reifenstein, Kleist Lab, KleistLab/DNS: First Release, Zenodo (2023); <https://doi.org/10.5281/zenodo.8130829>.

ACKNOWLEDGMENTS

We thank members of the Kleist and Hiesinger labs and I. Salecker for helpful discussions and G. Linneweber and R. Menzel for comments on the manuscript. We also thank T. Clandinin (Stanford), S.L. Zipursky (UCLA), and C. Desplan (NYU) for generously sharing reagents. **Funding:** This work was supported by DFG Research Unit 5289 *RobustCircuit* project Z1 (453877723, M.v.K. and P.R.H.), DFG grant 450430223 (M.v.K. and P.R.H.), DFG grant 443637483 (P.R.H.), DFG Excellence Center MATH+ (M.v.K.), and funding from the European Research Council under the European Union's Horizon 2020 research and innovation program (grant no. 1010191, P.R.H.). **Author Contributions:** E.A., E.T.R., M.v.K., and P.R.H. conceived the study and wrote the paper. All authors gave feedback on the manuscript. E.A., C.W., T.S., M.Ka., M.Ke., and A.K. performed all biological experiments. E.T.R. and M.v.K. performed all computational modeling. **Competing interests:** The authors declare that they have no competing interests.

Data and materials availability: All data are available in the main text or the supplementary materials. All original code has been deposited at Zenodo and is publicly available at <https://doi.org/10.5281/zenodo.8130829> (51). **License information:** Copyright © 2024 the authors, some rights reserved; exclusive licensee American Association for the Advancement of Science. No claim to original US government works. <https://www.science.org/about/science-licenses-journal-article-reuse>

SUPPLEMENTARY MATERIALS

science.org/doi/10.1126/science.adk3043

Materials and Methods

Figs. S1 to S19

Tables S1 to S3

References (52–62)

MDAR Reproducibility Checklist

Movies S1 to S9

Submitted 14 August 2023; accepted 1 February 2024

10.1126/science.adk3043